

# Space Weather®

## <del>-</del>

## RESEARCH ARTICLE

10.1029/2025SW004448

#### **Key Points:**

- This study constrains the occurrence and lifetimes of multi-MeV electrons during peak activity in solar cycle 22
- The slot region is repeatedly flooded with multi-MeV electrons, a phenomenon identified as a risk to slot region orbits during large storms
- Differences between the High Energy Electron Fluxometer loss timescales, previously reported timescales, and pitch angle diffusion theory are discussed

#### Correspondence to:

R. T. Desai, ravindra.desai@warwick.ac.uk

#### Citation:

Desai, R. T., Perrin, J., Meredith, N. P., Glauert, S. A., Ruparelia, S., & Johnston, W. R. (2025). Multi-MeV electron occurrence and lifetimes in the outer radiation belt and slot region during the maximum of solar cycle 22. *Space Weather*, 23, e2025SW004448. https://doi.org/10.1029/2025SW004448

Received 20 MAR 2025 Accepted 25 SEP 2025

#### **Author Contributions:**

Conceptualization: R. T. Desai, N P Meredith Data curation: S. A. Glauert, W. R. Johnston Formal analysis: R. T. Desai, J. Perrin, N. P. Meredith, S. Ruparelia Funding acquisition: R. T. Desai Investigation: R. T. Desai, J. Perrin, N. P. Meredith, S. Ruparelia Methodology: R. T. Desai, J. Perrin, S. A. Glauert, S. Ruparelia Project administration: R. T. Desai Resources: R. T. Desai, S. A. Glauert, W. R. Johnston Software: J. Perrin, S. Ruparelia Supervision: R. T. Desai Validation: R. T. Desai, N. P. Meredith, W. R. Johnston Visualization: R. T. Desai, J. Perrin.

© 2025. The Author(s).

This is an open access article under the terms of the Creative Commons

Attribution License, which permits use, distribution and reproduction in any medium, provided the original work is properly cited.

Writing - original draft: R. T. Desai

S. Ruparelia

## Multi-MeV Electron Occurrence and Lifetimes in the Outer Radiation Belt and Slot Region During the Maximum of Solar Cycle 22

R. T. Desai<sup>1,2,3</sup> D, J. Perrin<sup>1</sup>, N. P. Meredith<sup>2</sup> D, S. A. Glauert<sup>2</sup> D, S. Ruparelia<sup>1</sup>, and W. R. Johnston<sup>4</sup>

<sup>1</sup>Centre for Fusion, Space & Astrophysics, University of Warwick, Coventry, UK, <sup>2</sup>British Antarctic Survey, Cambridge, UK, <sup>3</sup>Blackett Laboratory, Imperial College London, London, UK, <sup>4</sup>Air Force Research Laboratory, Space Vehicles Directorate, Kirtland, AFB, USA

Abstract The Combined Release and Radiation Effects Satellite (CRRES) observed the response of the Van Allen radiation belts to peak solar activity within solar cycle 22. This study analyses relativistic and ultra-relativistic electron occurrence and loss timescales within the CRRES High Energy Electron Fluxometer (HEEF) data set, including during several strong and severe geomagnetic storms that all, remarkably, flooded the slot region with multi-MeV electrons. These allow the first definitive multi-MeV electron lifetimes to be calculated in this region and indicate an elevated risk to satellites in slot region orbits during periods of heightened solar activity. The HEEF outer belt loss timescales are broadly in agreement with those from later solar cycles, but differences include longer-lasting sub-MeV electrons near the inner region of the outer belt and faster-decaying multi-MeV electrons near geosynchronous orbit. These differences are associated with higher levels of geomagnetic activity, a phenomenon that enables the spread in the results to be parameterised accordingly. The timescales generally appear well-bounded by Kp-dependent theoretical predictions, but the variability within the spread is not always well-ordered by geomagnetic activity. This suggests the limitations of using pitch-angle diffusion to account for the decay of elevated electrons following geomagnetic storms, and the need for more sophisticated space weather indices for radiation belt forecasting.

Plain Language Summary The study found that during the peak of solar cycle 22, several large geomagnetic storms repeatedly filled the slot region between the inner and outer radiation belts with energetic electrons. This is significant because the slot region is typically thought to have lower radiation levels, and satellites operating there may be at increased risk during such events. As each 11-year activity cycle of the Sun is different, this helps to understand the potential risks to satellites during the present and future cycles. When comparing electron loss timescales (how quickly the particles disappear) to observations from later solar cycles, some differences were noted. These variations are likely due to enhanced geomagnetic activity during the observed period. The study also examined how geomagnetic activity relates to electron loss timescales. While theory based upon scattering the particles into the atmosphere generally matched the observed loss timescales, the relationship wasn't always straightforward. This suggests that our current understanding, and therefore forecasting, of hazardous electrons in the radiation belts may be incomplete.

## 1. Introduction

The Van Allen electron radiation belts consist of two concentric tori encircling the Earth with energies extending up to several MeV (van Allen, 1959). Satellites are designed to mitigate or avoid the impacts of these "killer" electrons which can lead to the triggering of phantom commands and component failure (e.g., Baker et al., 2013; Hands et al., 2018). The precipitation of energetic particles also directly influences the ionization and conductivities of the upper atmosphere, and its coupling back to the geospace environment (e.g., Orsolini et al., 2005; Roble & Rees, 1977). The dynamics of trapped relativistic electron populations are thus a primary focus of space weather research and forecasting efforts.

The electron radiation belts typically exhibit a two-belt structure, as commonly ordered by the Roederer (1970)  $L^*$  parameter. A stable so-called inner belt peaks between  $L^* \approx 1$ –2 (Selesnick et al., 2007) and a highly variable outer belt extends between  $L^* \approx 3$ –8 (Glauert et al., 2018). This canonical picture can however rapidly change during geomagnetic storms, with additional peaks in the relativistic particles flux, that is, new radiation belts, forming at various distances to the Earth, including inside the slot region. The first well-known example occurred

DESAI ET AL. 1 of 17

10.1029/2025SW004448

Writing – review & editing: J. Perrin, N. P. Meredith, W. R. Johnston

on 24 March 1991, where a large interplanetary shock near-instantaneously injected a new ultra-relativistic belt extending up to over 50 MeV inside the slot region (Blake et al., 1992; Hudson et al., 1997), and redistributed fluxes in the inner belt (Lozinski et al., 2025). Elevated energetic particles fluxes during this March 1991 event resulted in two satellite outages, and single event upsets and solar cell degradation on orbiting satellites (Ishikawa et al., 2013; Mullen et al., 1991; Shea & Smart, 1993). A further significant event occurred during solar cycle 23 following the Hallowe'en storms of 2003 where the outer belt reformed inside the slot region and into the inner belt as a result of enhanced convection and erosion of the plasmasphere (Baker et al., 2004). This similarly caused a satellite outage and extensive anomalies (Cho, 2005; NOAA Space Environment Center, 2004). This again occurred in solar cycle 25, when the Mother's/Gannon Day storm of May 2024 resulted in elevated fluxes forming inside the slot region (Li et al., 2025; Pierrard et al., 2024). The reordering of the outer belt into multiple distinct outer belts is also commonly occurring following geomagnetic storms (e.g., Baker et al., 2013; Chen et al., 2024; Pinto et al., 2018; Vampola, 1971).

Elevated electron fluxes in the inner magnetosphere, following geomagnetic storms, are observed to decay exponentially across timescales of days-weeks, a phenomenon associated with pitch-angle scattering into the atmospheric loss cone (Baker et al., 2004; Claudepierre et al., 2020; Meredith et al., 2006, 2009). This process provides a direct method to test diffusion theory (Albert, 2005; Glauert & Horne, 2005; Kennel et al., 1985; Lyons, 1974) and its application within 3-d radiation belt models (e.g., Fok et al., 2001; Glauert et al., 2014; Reeves et al., 2012; Shprits et al., 2009; Su et al., 2010). As a general overview the following plasma waves have found to be significant. Within the slot region, the dominant modes have been found to be plasmaspheric hiss (Lyons et al., 1972; Meredith et al., 2007), lightning-generated whistlers (LGW) (e.g., Lauben et al., 2001) and magnetosonic waves (Ma et al., 2016; Wong et al., 2022). Further out, hiss continues to play an important role for electron loss in the outer radiation belt both within the plasmasphere (Meredith et al., 2006; Summers et al., 2004) and in plasmaspheric plumes (Summers et al., 2008). In addition, electromagnetic ion cyclotron (EMIC) (Miyoshi et al., 2008; Ross et al., 2021) and whistler-mode chorus waves (Shprits et al., 2007; Wang et al., 2024; Wang & Shprits, 2019) and outward radial diffusion to the magnetopause (Mann et al., 2016; Shprits et al., 2006) may also contribute to electron loss in the outer radiation belt. Anthopogenic VLF whistlers and Coulomb collisions have also been found to be effective in the inner belt and slot region (Cunningham et al., 2018; Ripoll et al., 2014; Ross et al., 2019).

Multi-MeV electron loss timescales have been empirically calculated within a few studies but the energy discrimination has often been limited to a single energy channel (e.g., Baker et al., 2007; Ripoll et al., 2015; Seki et al., 2005; West Jr. et al., 1981). The Van Allen Probe electron lifetimes reported by Claudepierre et al. (2020) addressed this, determining decay rates within six differential energy channels extending from 1–4 MeV. This study provides analysis of multi-MeV electrons observed by Combined Release and Radiation Effects Satellite (CRRES) during the maximum of solar cycle 22, providing decay rates within six energy channels up to 4.55 MeV. Moreover, during the VAP mission multi-MeV electrons weren't seen inside  $L^* = 2.8$  (Baker et al., 2014) whereas in this study we find that CRRES regularly observed multi-MeV electrons inside the slot region. This enables the first calculation of well-resolved lifetimes in the slot region. To investigate the variability of the loss timescales we also parameterize the results by geomagnetic activity to perform an activity-dependent comparison of empirical electron loss timescales with predictions by PA diffusion theory.

The paper is structured as follows. In Section 2 we outline the concept of PA diffusion and the approach used to calculate the theoretical decay rates. In Section 3 we introduce the CRRES instrument and data set and the automated algorithm used to derive the empirical loss timescales. In Section 4 we then present the geomagnetic activity-dependent lifetime analysis of multi-MeV electrons during the severe geomagnetic storms that flooded the slot region and the automated retrieval of lifetimes through the entire data set. Section 6 then contrasts these with the theoretical solutions and previously reported loss timescales. Section 7 then summmarises the results of the study.

## 2. Pitch Angle Diffusion Theory

Pitch angle diffusion is caused by cyclotron and landau resonances. Under the assumption of quasi-linear theory of timescales longer than a drift-period, the pure PA diffusion equation for particle flux, f, as a function of time, t, and equatorial PA,  $\alpha_0$ , can be written as

DESAI ET AL. 2 of 17

$$\frac{\partial f}{\partial t} = \frac{1}{T \sin(2\alpha_0)} \frac{\partial}{\partial \alpha_0} \bigg|_{L^*, E} \left( T \sin(2\alpha_0) D_{\alpha\alpha} \frac{\partial f}{\partial \alpha_0} \right), \tag{1}$$

where  $D_{\alpha\alpha}$  represent PA diffusion coefficients and T ( $\alpha_0$ ) = 1.3–0.56 sin $\alpha_0$  as the latitude dependence of the bounce period. We can assume a basis of solutions given by these eigenmodes to be separable as  $f(\alpha, t) = A(\alpha)f(t)$ . The distribution is therefore represented by a superposition of exponentially decaying orthonormal eigen-states (O'Brien et al., 2008) and following Lyons et al. (1972), can be assumed to have,

$$f(t) = Ae^{(-t/\tau)},\tag{2}$$

for an equatorially mirroring PA distribution  $A(\alpha_0)$  and decay constant,  $\tau$ . This leaves

$$\frac{d}{d\alpha_0} \left( D_{\alpha\alpha} T \sin(2\alpha_0) \frac{dA}{d\alpha_0} \right) + \frac{T \sin(2\alpha_0)}{\tau} A = 0, \tag{3}$$

a second order difference equation that can be solved as a boundary value problem (Albert, 1994; Meredith et al., 2006) for a given PA distribution and as a function of chosen diffusion coefficients. The eigenvalues of the operator specify the time scales of the diffusion process (e.g., Albert & Shprits, 2009; Schulz & Lanzerotti, 1974) which Sturm-Liouville theory assumptions dictate are real and ordered (Claudepierre et al., 2022; O'Brien et al., 2008). The lowest order eigenvalues therefore yield increasingly longer timescales and these have appeared dominant within observations reported so far at both equatorial and high latitudes in the outer radiation belt (Baker et al., 2007; Claudepierre et al., 2020; Meredith et al., 2006). However, this may not always be the case if the timescales of the diffusion process are longer than the timescales acting and the higher-order eigenvalues act across similar timescales to those examined as in the inner slot region and inner radiation belt (Broll et al., 2023; Meredith et al., 2009). The exponentially decaying solution in Equation 2, allows empirical e-folding decays to be derived from observational data, as described in the next section, to serve as a direct comparison to these theoretical solutions.

In this study we utilize the Kp-dependent theoretical approach to Equation 3 of Glauert et al. (2024) which accounts for plasmaspheric hiss, upper/lower band chorus waves, EMIC waves, VLF transmitters, LGW and magnetosonic waves, derived within the Olson and Pfitzer (1977) field model. Glauert et al. (2024) used this approach to report loss timescales up to 1 MeV and at the single multi-MeV channel 2.6 MeV. In this study, we use this approach to show lifetimes within each of the six HEEF energy channels from 0.65 to 4.55 MeV. The hiss diffusion coefficients are derived from the wave model of Meredith et al. (2018) from  $2 \le L* \le 6$  using Dynamics Explorer, Double Star, Cluster, THEMIS, and VAP observations, and the PADIE code (Glauert & Horne, 2005). The chorus diffusion coefficients are derived using the observations reported by Meredith et al. (2020) for  $2 \le L \le 10$  based upon Dynamic Explorer, Double Star, THEMIS, and VAP, and the PADIE code. The VLF transmitter diffusion coefficients were derived by Ross et al. (2019) for L\* < 3 using VAP observations. The EMIC diffusion coefficients were derived by Ross et al. (2020, 2021) from  $3.25 \le L* \le 7$ using VAP observations. The LGW diffusion coefficients were calculated using PADIE for  $2 \le L \le 3$  based on the Green et al. (2020) VAP wave model and the densities of Ozhogin et al. (2012) from the IMAGE spacecraft. The magnetosonic diffusion coefficients are derived from Wong et al. (2022) using VAP observations. Pitch angle diffusion due to collisions with the atmosphere inside the loss cone is also incorporated as described in Selesnick (2016) for a tilted dipolar magnetic field with specified eccentricity.

#### 3. HEEF Data Set

#### 3.1. Instrumentation

The data used in this study is derived from the CRRES HEEF instrument which obtained measurements in an equatorial geostationary transfer orbit moving through radial distances of 1.05–6.26 Earth radii at an inclination of 18°, from 25 July 1990 till 12 October 1991 (Gussenhoven et al., 1996). The HEEF instrument (Dichter et al., 1993) was designed to measure the electrons in 10 channels up to 10 MeV with 10° half-angle PA spectra obtained through the spinning of the platform and the CRRES magnetometer. The instrument utilized two solid

DESAI ET AL. 3 of 17

Table 1
Mid-Point and Ranges of the High Energy Electron Fluxometer Energy Channels Used in This Study (Brautigam & Bell, 1995; McKellar, 1996)

Channel	0	1	2	3	4	5	6	7	8	9	10
$\mathbf{E}_{lower}$	0.50	0.85	1.25	1.70	2.10	2.50	2.90	3.30	4.10	4.95	6.66
$\mathbf{E}_{mid}$	0.65	0.95	1.60	2.00	2.35	2.75	3.15	3.75	4.55	5.75	7.50
$\mathbf{E}_{upper}$	< 0.80	<1.05	<1.70	< 2.10	< 2.50	< 2.90	<3.30	<4.10	<4.95	<6.6	< 8.55

state detectors and a bismuth germinate (BGO) crystal scintilator and an anti-coincidence plastic scintillator, to correlate a particle detection and determine energy and species. The HEEF instrument was extensively calibrated prior to launch (Dichter & Hanser, 1995) however, shortly after launch it became necessary to turn off a heater in the HEEF compartment with the result that HEEF operated at temperatures significantly different than planned. Since the operation of the BGO crystal scintillator is temperature sensitive, further calibration work on HEEF was completed using on-orbit data and laboratory calibration of a flight spare unit (Hanser, 1995). Despite this the complete unfolding and convergence of the in-flight data set was never accomplished with potential errors highlighted within the flux values (McKellar, 1996).

In 2014, further empirical calibration factors were applied to the HEEF data to re-establish the utility of this data set (Johnston et al., 2014a, 2014b). Starting from a data set version with temperature and dead-time corrections applied, further corrections were implemented, including removal of data with incomplete PA distributions and cross-calibration with the CRRES Medium Electron Analyzer (MEA) (Vampola et al., 1992). The resultant data set consists of one-minute averages of differential electron fluxes separated into 5° PA bins. The HEEF L\* values were calculated for Olson and Pfitzer (1977) quiet and epoch-appropriate IGRF 2010 (i.e., using IGRF 2010 to compute values for 1990–1991). The AE9/AP9 neural net-based interpolation algorithm was used to reduce computation times (Ginet et al., 2013). Table 1 outlines 10 differential energy channels, eight of which are intrinsic to the instrument mode of operation and two additional differential channels (0.65 and 0.95 MeV) derived from differencing pairs of integral channels (Brautigam & Bell, 1995). For further description of the cleaning of the data set and the contents, the reader is referred to Johnston et al. (2014a, 2014b).

## 3.2. Deriving Empirical Loss Timescales

Empirical electron lifetimes can be calculated using the same solution to Equation 1 through fitting the timescale,  $\tau$ , in Equation 2 directly to the HEEF data. We use a linear fit to the natural logarithm of the data to reduce interference from the largest fluxes. The derivation of electron lifetimes utilizes daily averaged electron fluxes and their temporal evolution within individual energy bins over extended periods. The data does not consist of daily averages, rather the average of each pass through 0.1 L\* shell ranges. In the outer belt and slot region the electron distribution functions,  $A(\alpha_0)$ , are summed between local pitch angles 60–120° to maximize counts and taken for observations between  $\pm 15^\circ$  magnetic latitude. In the inner belt, 90° PA fluxes are used only, as the lifetimes here are highly pitch angle dependent. The data is smoothed over a period of 1–2 days and decays fitted using the exponential function over periods not less than 5 days, although the results are relatively insensitive to these specific parameters. To determine the quality of the fits we used the Pearson correlation coefficient, a value between -1 and 1, 0 being no correlation, -1 being a perfect negative correlation and 1 a perfect positive, with a threshold of -0.95 for determining an accurate timescale. Following periods of exponential decay, the flux levels exhibit significant variations likely representing a balance of production and loss and radial transport and the assumptions behind using Equation 2 are no longer valid.

This process is automated with predefined criteria specifying the determination of a fit to a decay timescale. For automatic fitting, each flux data point is sequentially selected to be the starting point for a fit, with the initial end point determined by the given minimum fit range value. The resulting fit is used to find the Pearson coefficient and standard deviation. If a fit is found, the algorithm returns a negative Pearson coefficient with a value less than the threshold, the end point is incremented, with this process continuing until the Pearson value is no longer lower than the threshold. This incrementation of the fit length is continued within a given tolerance of Pearson values to avoid local minima. If the fit returns a Pearson with a value greater than the threshold, both the start and end points

DESAI ET AL. 4 of 17

from https://agupubs.onlinelibrary.wiley.com/doi/10.1029/2025SW004448 by NICE, National Institute for Health and Care Excellence, Wiley Online Library on [17/10/2025]. See the Terms

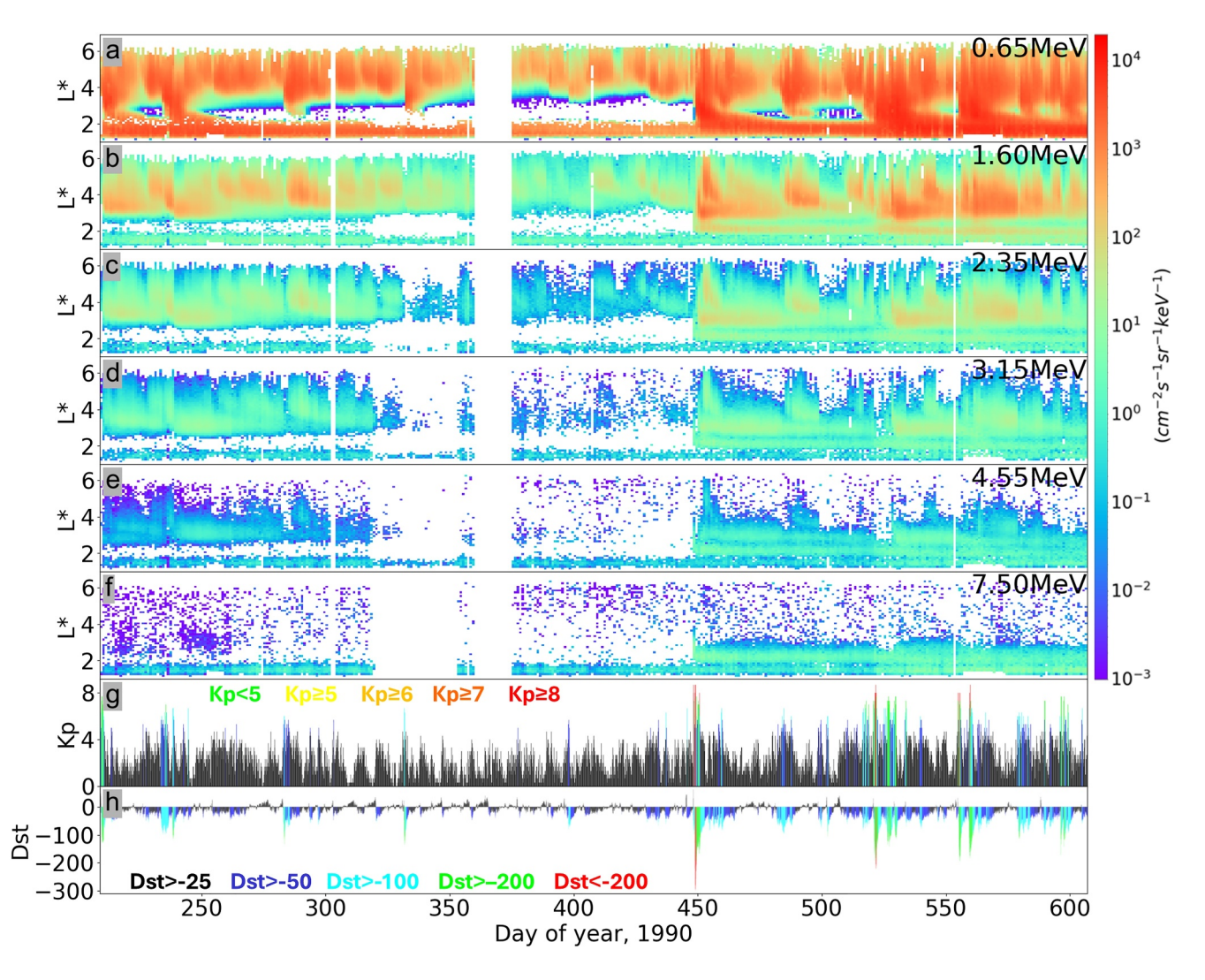


Figure 1. High Energy Electron Fluxometer daily averaged differential number flux at each second energy channels outlined in Table 1 in subplots (a–f) throughout the Combined Release and Radiation Effects Satellite mission. Subplot (g) and (h) show the respective corresponding Kp and Dst indices.

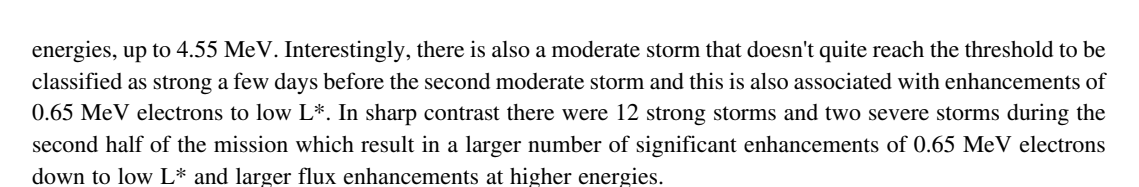
are incremented and the fitting process is repeated on the new data range until the Pearson value becomes less than the threshold, that is, a new decay is found.

## 4. Geomagnetic Storms in the CRRES Era

Figure 1 shows the HEEF data throughout the CRRES mission ordered by day numbers continuous from day 1=1 January 1990. Specifically, we show the averaged electron differential number flux as a function of L\* and time at energies of (a–f) 0.65, 1.60, 2.35, 3.15, 4.55, and 7.50 MeV. In the absence of continuous upstream solar wind measurements, panels (g) and (h), respectively, show a trace of the Kp and disturbance storm time (Dst) indices as a measure of the surrounding geomagnetic activity. The Kp indices are ordered according to the NOAA geomagnetic storm scales; Kp < 5, Kp  $\geq$  5 (G1), Kp  $\geq$  6 (G2), Kp  $\geq$  7 (G3) and Kp  $\geq$  8 (G4), and the disturbance storm time (Dst) indices according to the storm definition of Loewe and Prölss (1997); Dst < -30 nT (weak), Dst < -50 nT (moderate), Dst < -100 nT (strong) and Dst < -200 nT (severe). As CRRES ended in October 1991 it did observe any great/extreme events defined by Kp = 9 (G5) or Dst < -350 nT, although one did notably occur one month after the mission ended, on 9–10 November 1991, where Dst reached -354 nT (Cliver et al., 2009).

Figure 1 shows during the first half of the mission there were four strong storms and these are all associated with enhancements of 0.65 MeV electrons down to low values of  $L^*$  with some events extending deep into the slot region and even the inner radiation belt. These storms tend also to be associated with flux enhancements at higher

DESAI ET AL. 5 of 17



The Kp index notably shows different scalings to the Dst in that in the second half of the mission three storms reach Kp = 9- (G4), an equivalence between them in contrast to the Dst index showing the single event on March 1991 reaching an intensity significantly greater than the others. The Kp index also reveals several peaks within each of the three G4 storms, for example, in March 1991 showing two Kp = 9- peaks corresponding to a first large compression reported early on 24 March (Blake et al., 1992) where the magnetopause was pushed inside geosychronous orbit for over five hours (Elphic et al., 1991) and then a further large compression late on 24 March and 25 March, reported to drive large magnetopause oscillations near geosychronous orbit (Cahill & Winckler, 1992; Desai, Freeman, et al., 2021). The Kp index is a mid-latitude metric and this could be caused by motion of the auroral oval due to dynamic pressure enhancements associated with successive coronal mass ejections (Koehn et al., 2022). The Dst index is conversely an equatorial index, associated with southward directed interplanetary magnetic fields and build-up of the ring current, and this therefore captures the geomagnetic response across longer time-periods. Several studies have highlighted that radiation belt flux variations may be better correlated with the Kp index (Borovsky & Shprits, 2017; Wang et al., 2024).

Significant attention has been devoted to deriving the properties of the interplanetary shock that struck on 24 March 1991 (day 447) due to the rapid nature that the slot region was filled with indications that it reached 1,500 km/s at the Earth (Blake et al., 1992; Elkington et al., 2004; Hudson et al., 1997; Li et al., 1993). The June storm (day 524) and subsequence disturbances persisted for nearly 20 days, and featured four geomagnetic storms in total of varying intensity, the magnetospheric responses identified as likely reflecting successive high-speed solar wind structures and periods of strong southward solar wind magnetic field (Gao et al., 1997). Although the solar wind conditions have not been analyzed, the July 1991 (day 554) storm was similarly inferred to derive from a large enhancement in dynamic pressure which pushed the magnetopause inside geosynchonous orbit for 3 hr, and large sudden storm commencement electric field that induced notable effects in the ionosphere (Burke et al., 2000; Wilson et al., 2001). The storm of 04 June 1991 (day 520) received less attention, but is listed 57 in the most extreme storms between 1868 and 2010, as ordered by the AA index (Vennerstrom et al., 2016). This is two places above the 24 March 1991 event which sits at 59 and the July event is not listed. This AA-ordering further highlights inconsistencies between different geomagnetic indices. The lack of continuous upstream solar wind observation in 1991, with only intermittent observations from IMP8 when orbiting in the solar wind, unfortunately precludes further analysis of the upstream drivers of these storms observed by CRRES.

The outer radiation belt appears highly variable throughout the CRRES mission driven by elevated geomagnetic activity. Following the geomagnetic storm of 24 March 1991, the multi-MeV electrons in the outer belt are separated into two further belts as examined by Kellerman et al. (2014) at lower energies. The corresponding energy and PA spectra are coherent up to 4.55 MeV and this multi-belt structure therefore also manifests at multi-MeV energies. The flux levels at low counts appear highly variable, and we thus determine an approximate "noise floor" in the data below which we do not try to interpret signals as genuine. This high noise floor, unfortunately, precludes the analysis in the study of the two highest energy channels 9 and 10, 5.75 and 7.5 MeV respectively, in this study.

Figure 2 shows HEEF energy and PA distributions corresponding to the data in Figure 1 during three large geomagnetic storms and a lesser fourth storm on 26 August 1991, day 238. For each of these, the spectra are displayed at four distinct radial distances, in the inner belt at  $L^* = 1.5$ , in the heart of the slot region at  $L^* = 2.5$  and then in the outer belt at  $L^* = 3.5$  and  $L^* = 4.5$ . In Figures 1 and 2, an inner electron radiation belt is visible at  $L^* < 2$  for the whole mission. In the lowest-energy channel 0, centered at 0.65 MeV, the dynamics of this inner belt correlate well with enhanced fluxes at higher L shells. The PA spectra at energy channel 0 (0.65 MeV) MeV at  $L^* = 1.5$  in Figure 2 also agrees well with expectations appearing symmetric about 90°. The next energy channel 1 (0.95 MeV) is, however, devoid of fluxes in the inner belt. The higher energy channels do display counts here, but the non-uniform spectra are suggestive that this is proton contamination at multi-MeV energies in the inner zone. We are therefore unable to ascertain whether MeV and multi-MeV electrons appeared within the inner belt during the CRRES mission.

DESAI ET AL. 6 of 17

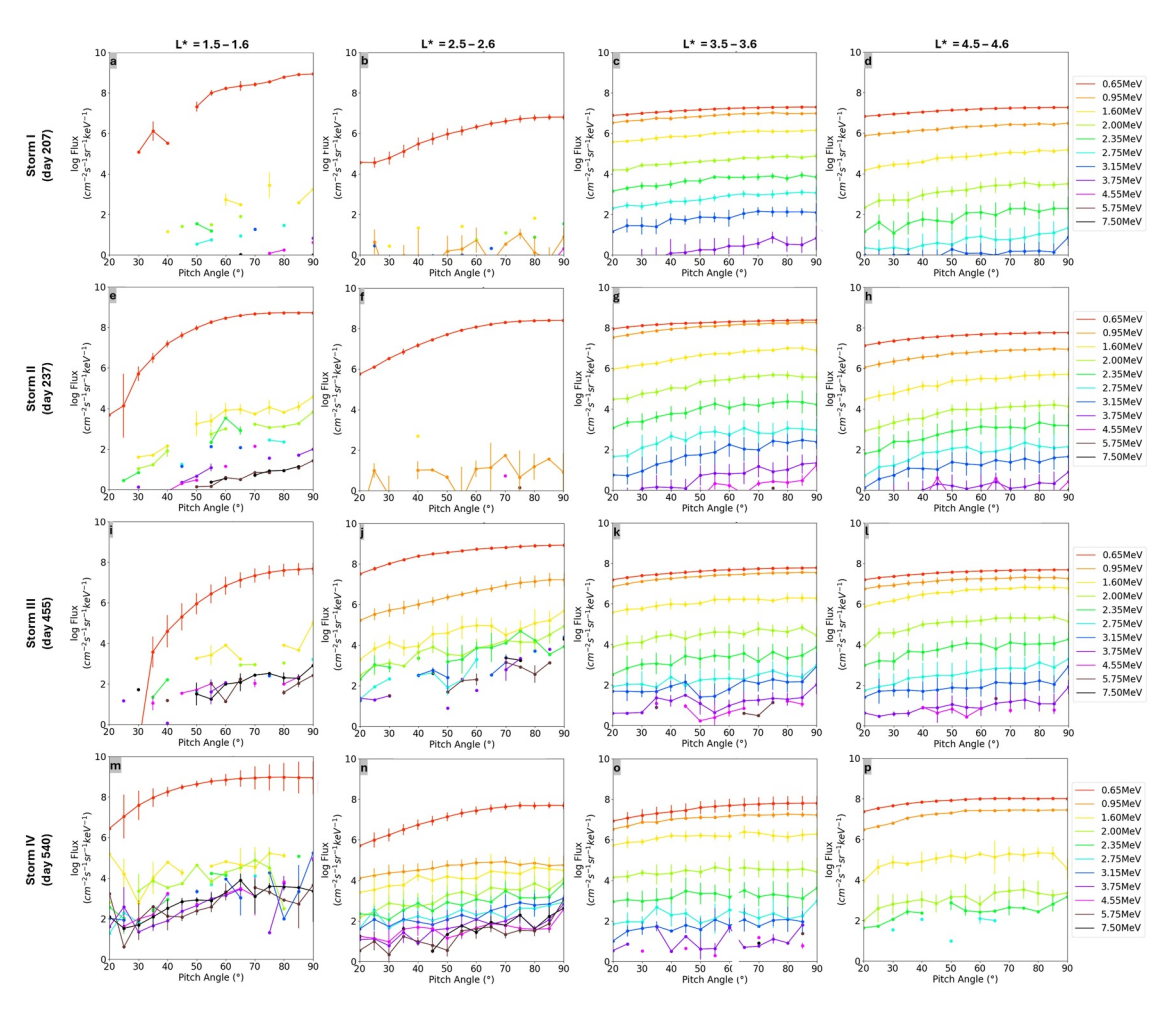


Figure 2. Pitch angle distributions at different L\* shells, used as a measure of identifying coherent or contaminated electron spectra. Day 207 = 26 July 1990; day 237 = 25 August 1990; day 455 = 31 March 1991; day 540 = 24 June 1991.

Within the slot region, see  $L^* = 2.5$  panel in Figures 1a–1f and 2, elevated flux levels start after 24 March 1991 (day 448) and extend right through to the end of the mission. The fluxes for the few orbits surrounding the injection of this new belt on day 448 (Blake et al., 1992) are not present in the data set due to the cleaning procedures applied (Johnston et al., 2014a, 2014b) but the decay of this belt is visible following day 450. The corresponding energy and PA spectra in Figure 2j show coherent observations up to several MeV inside the slot region and throughout the outer belt. The further geomagnetic storms after days 524 and 554 in Figure 1 also produce elevated fluxes in the slot region of a similar or greater magnitude to those deriving from the 24 March 1991 event, with fluxes comparable to those in the outer belt. The extended June 1991 disturbances (Gao et al., 1997) correlates with an increase in the slot region electron flux over an extended time period, in contrast to the March 1991 more sudden increase. The July increase similarly occurs over an extended period.

The Kp reaches similar magnitudes for these events, but the Dst index is significantly lower. These events are notable in that during solar cycle 24, multi-MeV electrons were unable to penetrate below  $L^* = 2.8$  (Baker et al., 2014), with great solar activity in 2003 (Baker et al., 2004) and 2024 (Li et al., 2025; Pierrard et al., 2024) required to overcome this. These events enable us to calculate slot-region loss timescales at multi-MeV energies, something that was not possible during the Van Allen probe era.

To examine the persistence of the multi-MeV electrons within these slot-filling events, Figure 3 shows the data within an  $L^* = 0.1$  bin, centered at  $L^* = 2.5$ , in each energy channel up to 4.55 MeV. The first storm only displays data at the lowest energy channels but three decay periods following storms in the latter part of the mission are fitted to at all energy channels, overlaid as red lines, with Pearson correlation coefficients all lower than -0.95.

DESAI ET AL. 7 of 17

15427390, 2025, 10, Downloaded from https://agupubs.onlinelibrary.wiley.com/doi/10.1029/2025SW00444 by NICE, National Institute for Health and Care Excellence, Wiley Online Library on [17/1/2025]. See the Terms and Con

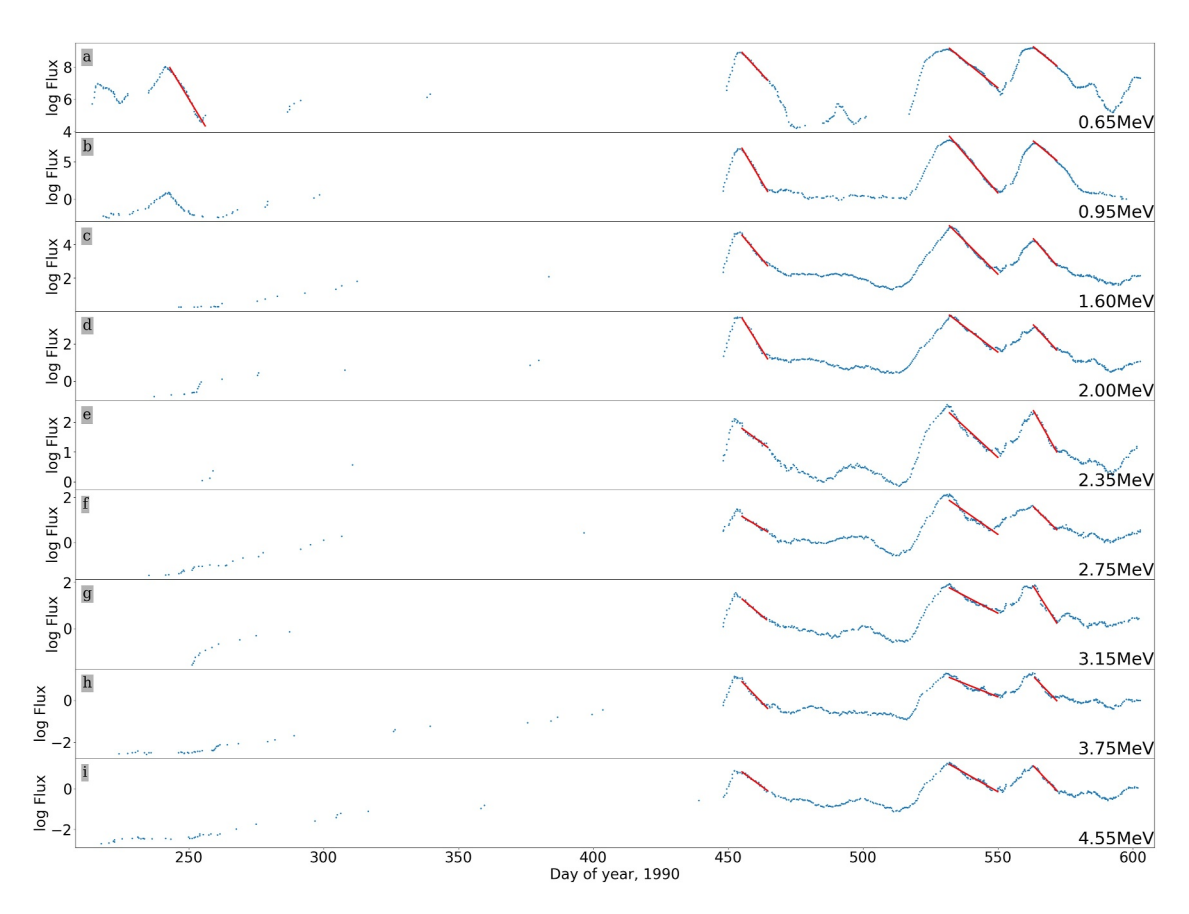
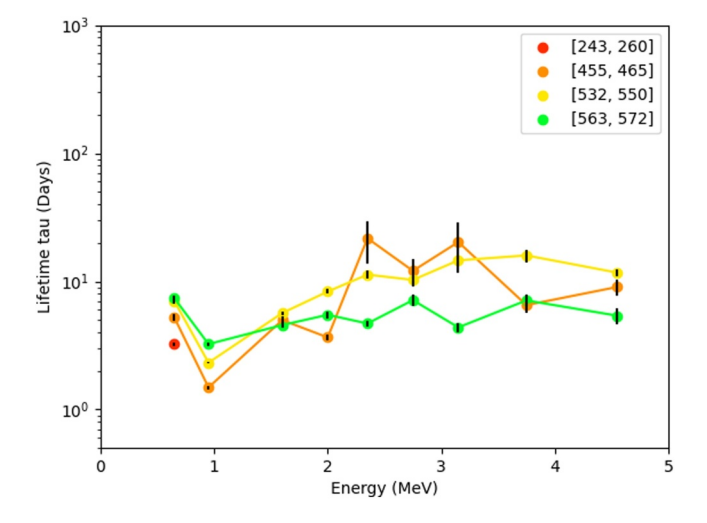


Figure 3. Slot region electron differential number flux at  $L^* = 2.5$  as a function of day number for the entire Combined Release and Radiation Effects Satellite mission (a–i) Shows 0.65, 0.95, 1.60, 2.00, 2.35, 2.75, 3.15, 3.75, and 4.55 MeV electrons, within a  $L^* = 0.1$  bin. Fitted exponential decays are overplotted in red for a minor storm at the storm of the mission and three severe storms during the latter half.



**Figure 4.** Electron loss timescales in the slot region at  $L^* = 2.5$ –2.6, as a function of energy for four doy time-periods during the Combined Release and Radiation Effects Satellite mission noted in the legend.

Figure 4 shows the resultant lifetimes as a function of energy from these periods. The trends show increased lifetimes at sub-MeV energies which decreases to a minimum near 1 MeV associated with increased PA diffusion into the loss cone (Glauert et al., 2024, see Figure 3 therein). The lifetimes then increase again and level out at multi-MeV energies.

## 5. HEEF Electron Lifetimes

To examine electron lifetimes throughout the CRRES era, Figure 5 then shows data across a range of L shells in the lowest energy channel, 0.65 MeV. The fits are once again overlaid on top of the data. The automated algorithm returns increasing numbers of fits at the intermediate L shells examined, overall visibly well-capturing exponentially decaying fluxes. A few flux decreases can however also be seen to be missed. In some instances, for example, Figure 5d, it might appear that there are two stages to the decay process, for example, in Figure 5g after day 450. These often appear as a shallow gradient followed by a greater decrease in the differential number flux. Further non-uniform decays are evident near the peak fluxes themselves over shorter time periods, with notably rounded structures at the lower L shells. This may in part be due to increasing production close to the initial event, varying geomagnetic activity levels during the decay, or potentially different eigenmodes dominating the PA diffusion. At the lowest L shells, the electron fluxes decay over extended periods of tens-hundreds of days. The

DESAI ET AL. 8 of 17

15427390, 2025, 10, Downloaded

from https://agupubs.onlinelibrary.wiley.com/doi/10.1029/2025SW004448 by NICE, National Institute for Health and Care Excellence, Wiley Online Library on [17/10/2025]. See the Term

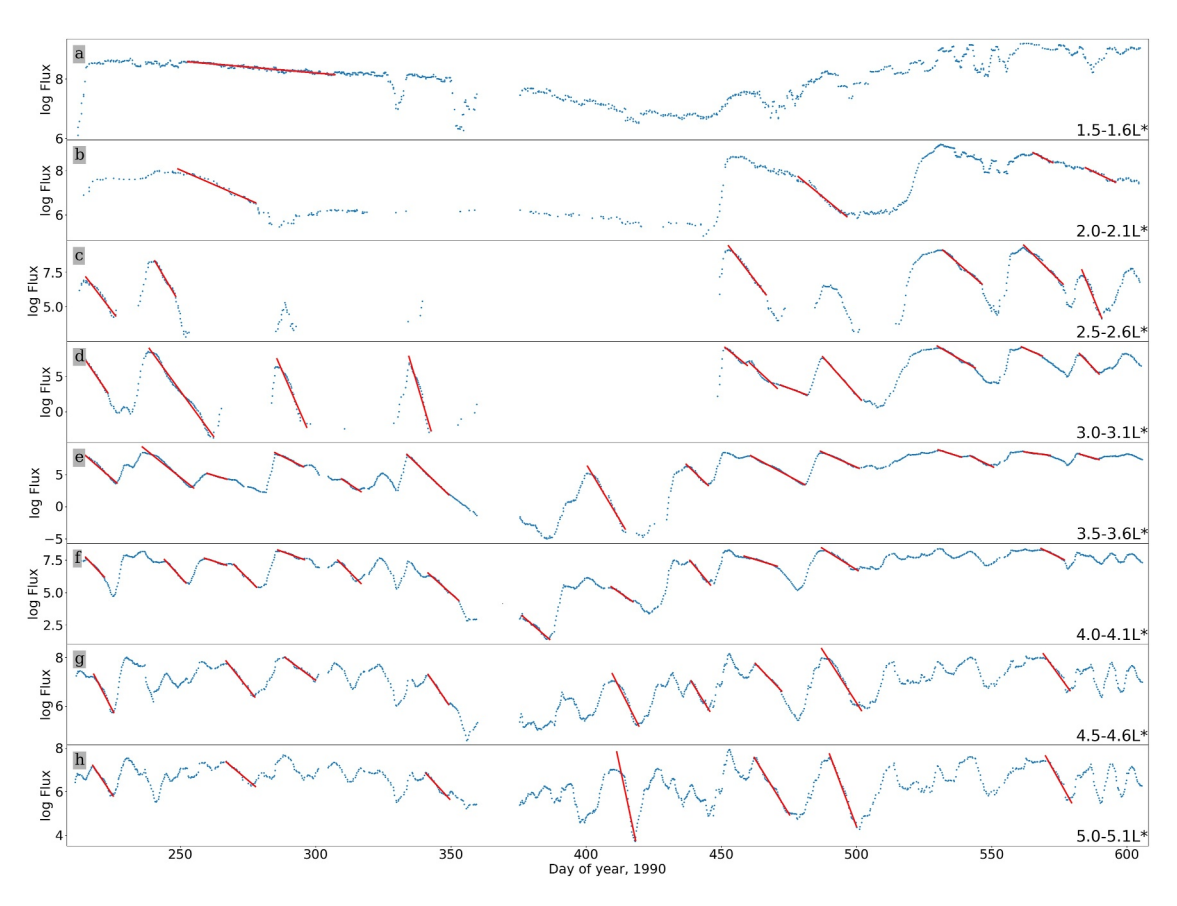


**Figure 5.** The 0.65 MeV electron energy number flux as a function of day number for the entire Combined Release and Radiation Effects Satellite mission for (a–g) 1.5–1.6 L\*, 2.5–2.6 L\*, 3.0–3.1 L\*, 3.5–3.6 L\*, 4.0–4.1 L\*, 4.5–4.6 L\* and 5.0–5.1 L\*. The fitted exponential decays are overplotted in red.

automated nature of the algorithm struggles with this extended period due to a shorter minimum fit window required to be defined to resolve the shorter timescales at larger L shells. The fluxes also exhibits significant short-term variability in the belt, on the order of several days. While the PA spectra in Figure 2 appear coherent, we restrict our lifetime calculations in this region to a single event between day 265 and 310 at 0.65 MeV.

The decay periods are well-represented by the exponential fits in the region  $3.0 \le L^* \le 4.5$ . At  $L^* \ge 5$ , only a few fits are visible. This may in part be due to the algorithm being difficult to optimize for such a wide spread in lifetimes where, at these greater radial distances, further transport processes associated with radial diffusion (Su et al., 2010), drift shell splitting (Sibeck et al., 1987) and drift orbit bifurcations (Desai, Eastwood, et al., 2021) become significant.

Figure 6 displays the results across all  $L^*$  shells in the slot region and outer belt in each energy channel with each fit colored according to its mean Kp index across the entire decay period. This allows analysis of the conditions that exist during the quiet time following the event and determine the electron lifetimes. The average fit at each 0.1  $L^*$  bin is also shown as a black line together with error bars representing the standard deviation. At the lowest  $L^*$  shells at the edge of the inner belt, the lifetimes of the 0.65 MeV electrons rapidly increase upward. The inner belt lifetimes are not discussed further here with regards to geomagnetic activity, due to their PA dependence, but are discussed in the subsequent section. Decreased slot region lifetimes between  $L^* = 2-3$  appear at this energy, as in Figure 3, before the lifetimes increase to another smaller maximum near  $L^* = 4$ .

The lifetimes of the 0.95 MeV electrons are lower than those of the 0.65 MeV electrons near  $L^*=4.0$  but this trend does not extend into the slot region where the reverse is true. There is a further peak near  $L^*=2.5-3$  but this is due to a large spread in the data here. At energies greater than 1 MeV, the peak lifetime in the outer belt moves inward with increasing energy from  $L^*\approx 4.5$  at 1 MeV down to  $L^*\approx 3$  at 4.55 MeV. The location of the shortest lifetimes in the slot region fluxes also move inwards, with increasing energies displaying longer lifetimes.

DESAI ET AL. 9 of 17

15427390, 2025, 10, Downloaded

from https://agupubs.onlinelibrary.wiley.com/doi/10.1029/2025SW004448 by NICE, National Institute for Health and Care Excellence, Wiley Online Library on [17/10/2025]. See the Terms

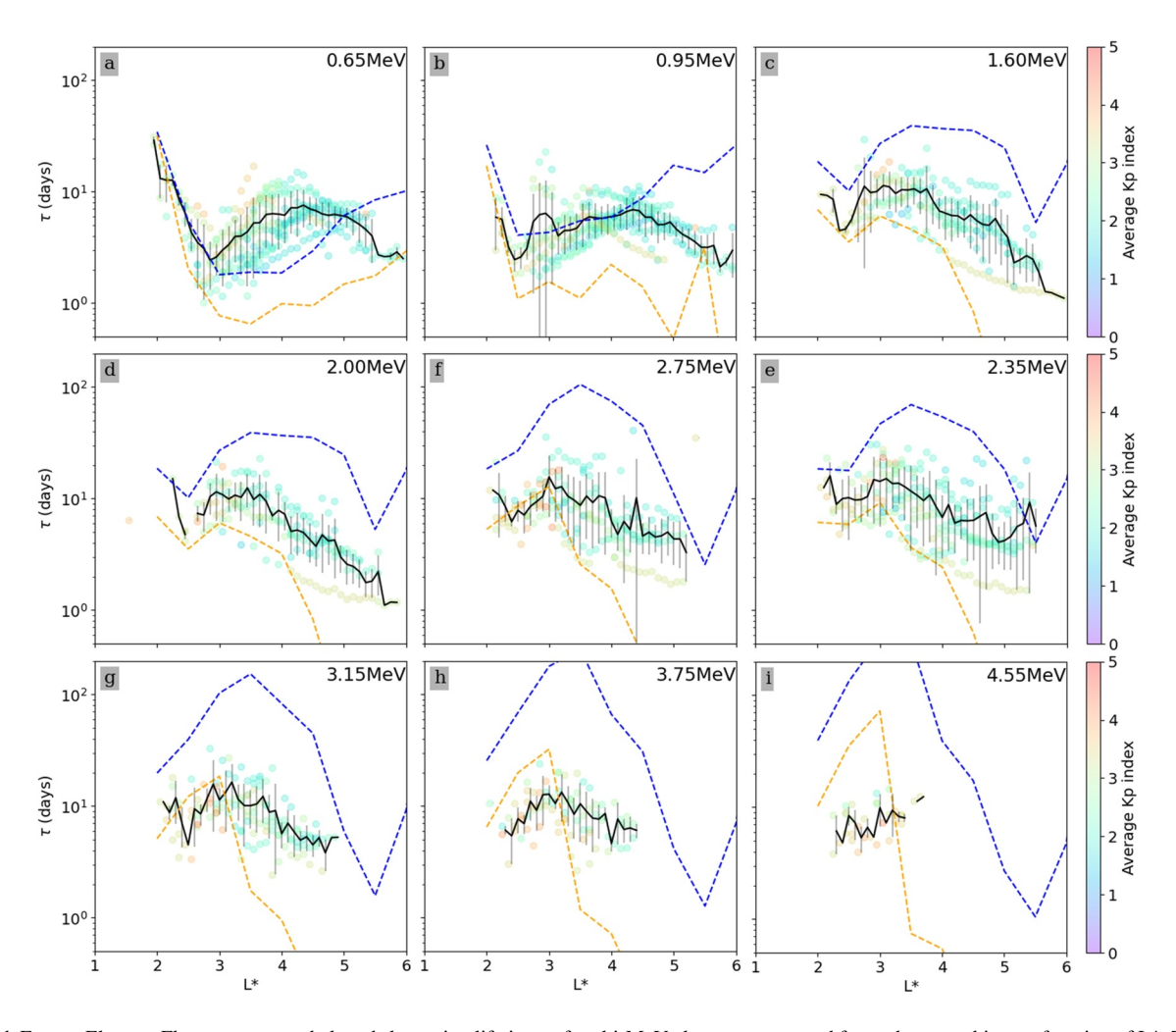


Figure 6. High Energy Electron Fluxometer outer belt and slot region lifetimes of multi-MeV electrons presented for each energy bin as a function of  $L^*$ . The raw data are colored according to the average Kp index during the decay period, the black line shows the average fit with error bars showing the standard deviation of calculated lifetimes. Pitch angle diffusion theoretical predictions are shown at Kp = 0–1 and 4–5.

In addition to the average trends, the Kp values of each fitted lifetime indicate how the decays scale with geomagnetic activity. At higher  $L^*$  shells, that is, greater than  $L^* = 3$ , elevated geomagnetic activity appears to drive fast losses with some of the shortest timescales showing Kp values near 5. At the lower  $L^*$ 's, however, and particularly at the lowest energy channel of 0.65 MeV, high Kp values often correspond to longer decay timescales. High Kp scenarios will still result in injections from the tail and subsequent acceleration of energetic particles and this trend therefore might be explained by sustained production of electrons occurring alongside PA scattering, a phenomenon which preferentially affects lower energies. This is further discussed in Section 6.

## 6. Comparisons and Discussion

To compare the HEEF results with PA diffusion theory, the PA diffusion lifetimes described in Section 2 are also plotted in Figure 6 with dashed lines representing decays for minimum and maximum Kp levels of 0–1 and 4–5 respectively. The average HEEF results are also plotted in Figure 7 with further empirical results from other spacecraft. These include coinciding measurements from the CRRES-Medium Energy Analyzer (CRRES-MEA) (Meredith et al., 2006), from VAP between 2012 and 2019 (Claudepierre et al., 2020), from ACE/DEMETER from year 2000 (Benck et al., 2010) and from SAMPEX in 2003 (Meredith et al., 2009). All the lifetimes are interpolated to the HEEF energy channels with the 2–6 MeV SAMPEX data judged to best represent 2.35 MeV, see for example, the relative fluxes in Figure 2. The CRRES and theoretical results are expressed in terms of L\* whereas the further empirical results are expressed in terms of dipole L shell. The subsequent discussion utilizes

DESAI ET AL. 10 of 17

15427390, 2025, 10, Downloaded

from https://agupubs.onlinelibrary.wiley.com/doi/10.1029/2025SW004448 by NICE, National Institute for Health and Care Excellence, Wiley Online Library on [17/10/2025]. See

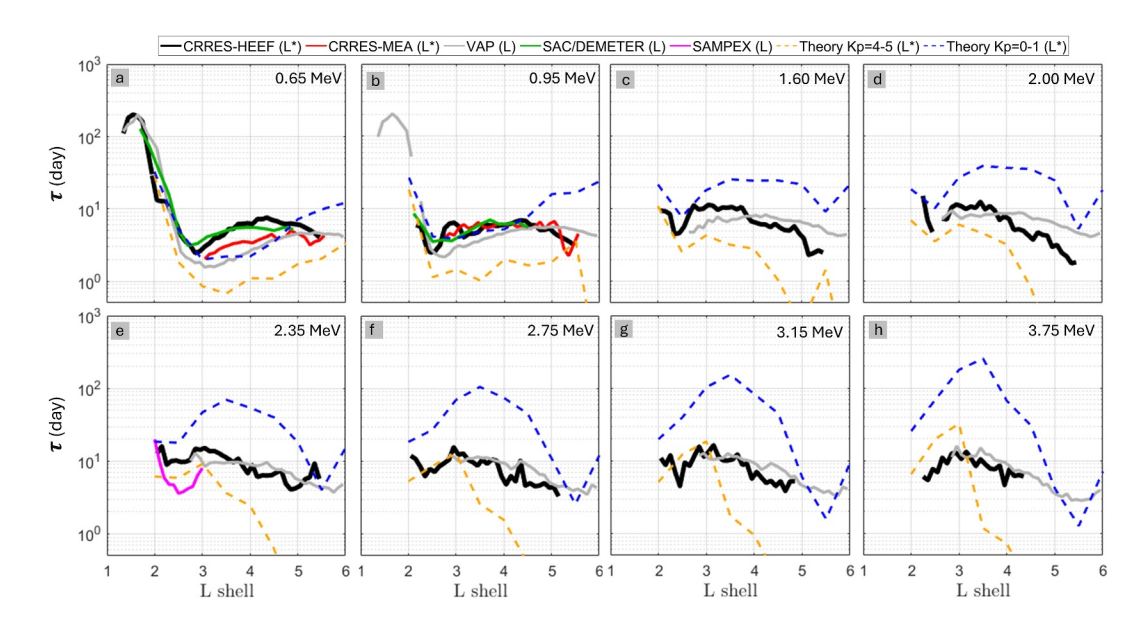


**Figure 7.** Experimental and theoretical electron lifetimes as a function of L shell in the outer belt and slot region for (a–h) 0.65, 0.95, 1.60, 2.00, 2.35, 2.75, 3.15 and 3.75 MeV electrons respectively. The black, red, gray, green and pink traces represent the experimental lifetimes derived from the CRRES-HEEF (this study), CRRES-MEA also from cycle 22 (Meredith et al., 2006), VAP from cycle 24 (Claudepierre et al., 2020), and SAC/DEMETER (Benck et al., 2010) and SAMPEX (Meredith et al., 2009) data sets from cycle 23. The dashed blue and orange traces represent the pitch angle diffusion theoretical lifetimes for quiet and high geomagnetic activity, respectively. All data is interpolated to the High Energy Electron Fluxometer (HEEF) energies, whereas the SAMPEX 2–6 MeV data are associated with the 2.35 MeV HEEF channel.

the term L shell when comparisons are between lifetimes utilizing these different measures of the radial location of electron orbits.

In Figure 6, the PA diffusion theory matches the observed trend of increased lifetimes near the inner belt at 0.65 MeV and depressed lifetimes in the slot region. In the inner part of the outer radiation belt, the quiet-time theoretical lifetimes at this energy are a factor of two or more smaller than the observed lifetimes in the region 3.2 < L\*< 4.6. These larger HEEF lifetimes are similar to those observed by SAC/DEMETER in cycle 23 (Benck et al., 2010) and also by ATS-1 (Vampola, 1971) in cycle 20 see Claudepierre et al. (2020, Figure 2f therein). This however is not observed in the VAP lifetimes. Further examination of Figure 6 reveals a cause of this discrepancy. The underlying HEEF fits, most visibly between L\*=3-4, feature a clustering of lifetimes at the lower lifetimes ranges, similar to those reported by the MEA and closer to those observed by VAP. However, an additional clustering above this demonstrates a bi-modality within the data set, with this second cluster corresponding to higher Kp values. This bimodality is also identifiable in the underlying fits on Figures 5e and 5f where many of the fitted lifetimes have shallower gradients.

The consequent differences in the average lifetimes in Figure 7a may therefore have been caused by differing levels of geomagnetic activity, with CRRES having observed an average Kp index of 2.67 compared to the VAP average of 1.67. This can be explained through three distinct mechanisms. Firstly, the intensity of geomagnetic storms were significantly greater in solar cycle 22 compared with solar cycle 24. These, during the latter half of the mission, indeed appear to be associated with the slower decays in Figure 5. These intense and longer lasting events influence the average Kp indices of a decay and thus skew the decay rates to higher Kp values, producing a "left-right" Kp bias as indeed shown by Meredith et al. (2006, Figure 6 therein). Secondly, disturbed geomagnetic conditions would more frequently reoccur during a decay period. This is visibly consistent with several of the decays observed, see for example, the decays days 270 and 295 in Figures 5f and 5g where large injections/enhancements occur during the decay period. Thirdly, it is well-known that typical solar wind parameters have declined significantly over the past 50 years, with differences between the 1970–1990's and 2010's having been highlighted as high as tens to over 50 percent (McComas et al., 2013). Such long-term trends in the radiation belts are difficult to study due to their inherent variability, and the inconsistency of dedicated missions, but the

DESAI ET AL. 11 of 17

longitudinal comparison between CRRES and VAP data, may enable such trends to be identified. Higher ambient solar wind driving might therefore have resulted in enhanced background levels of magnetotail loading and substorms injections. In addition, each of the above three points might also cause the plasmasphere/plasmaspheric hiss to extend to lower *L* shells during the CRRES era than during the VAP era. Lower energies are particularly affected by this loss mechanism, as found by the evolution of the energy spectra within VAP and CRRES observations (Johnston et al., 2010; Zhao et al., 2019).

The bimodality in the decays rates is less apparent in the lifetimes beyond  $L^* = 4$ , with the high Kp lifetimes now more often lower than the low Kp lifetimes and the average even lower than the VAP observations beyond  $L^* = 5$ . The CRRES-MEA (Meredith et al., 2006) lifetimes are lower than the HEEF lifetimes in the outer belt between L = 2-4 although are higher than determined by VAP. The reason behind the differences with the MEA data set is initially surprising given the HEEF and MEA data sets have been cross-calibrated (Johnston et al., 2014a, 2014b). Comparisons between the Meredith et al. (2006) fits at the MEA energy channel of 0.604 MeV (not shown) and the HEEF energy channel of 0.65 MeV in Figure 5, indicate that the HEEF fitting algorithm skews toward longer fits. This is evident near days 270, 495 and 520 in Figure 5f as these events feature some intrinsic variability in the fluxes, and Kp and DST indices, see Figure 1, but which overall are still well-approximated by periods of exponential decay if the algorithm is able to move past local minima in the Pearson values. This type of discrepancy may also explain further differences between the various studies reporting electron loss timescales. A further factor to be considered is that Brautigam and Bell (1995) adopt an energy span of 0.50-0.80 MeV for HEEF energy channel 0 and the electron lifetimes derived from HEEF for 0.65 MeV are therefore influenced by longer lifetime electrons than the MEA lifetimes. This is the energy-dependent decay seen in Meredith et al. (2006) and Zhao et al. (2019), i.e. as lower energy electrons are depleted the higher energy ones will dominate and may thus influence the lifetime more.

It should be noted that Claudepierre et al. (2020) identify contamination due to Brehmstrahlung from higher energy electrons as a further potential cause of these longer lifetimes in the MEA and SAC/DEMETER data sets. As CRRES did not downlink the data required to identify and correct this effect, it is not possible to ascertain the extent to which HEEF was affected via the same method as VAP. However, we don't tend to observe features at 0.65 MeV similar to those reported by Claudepierre et al. (2020) at 0.6 MeV in the VAP uncorrected data, which tend to show two different decay periods when the contamination is present, with a rapid initial decay and then a more gradual decay. This suggests that contamination from Bremsstrahlung is not so significant for the HEEF data. The 0.65 MeV lifetimes also peak beyond  $L^* = 4$ , whereas the multi-MeV lifetimes peak below  $L^* = 3$  and so the multi-MeV electrons are not directly correlated with the elevated lifetimes at 0.65 MeV. The HEEF and VAP lifetimes at higher energies also show good agreement, see subsequent discussion, and the HEEF lifetimes are actually shorter in the outer belt, consistent with higher accompanying geomagnetic activity.

In the inner belt, the decay timescales match closely with the VAP decay timescales, which were also determined for 90° flux. These elevated fluxes in the HEEF data set, see Figure 5a, appear to have been caused by storms at or prior to the start of the mission followed by relatively quiet conditions which allow their decay timescales to be calculated across this period. These loss timescales approach 200 days and is also evident in that during the second half of the mission, see again Figure 5a where geomagnetic activity was higher, the 0.65 MeV flux is unable to decay and appears to be largely on an upward trend from around day 450–550. This points to the controlling influence of slot region fluxes on electron flux levels in the inner belt.

At 0.95 MeV, Figures 6b and 7b, the theory bounds many of the fitted lifetimes but is lower than the observations when scaling by geomagnetic activity with half the fitted lifetimes outside the upper bound predicted by theory. The HEEF, MEA and SAC/DEMETER observations however show similar lifetimes at all L shells. The VAP lifetimes appear slightly lower, consistent again with the lower geomagnetic activity argument discussed previously with reference to Figure 7a. At 1.60 MeV, Figures 6c and 7c, the HEEF and VAP observations show similar average values at L shells of 4.5–5.5 but further in, the HEEF results decay more slowly in-line with the previously discussed high Kp-associated decays. This trend is similar at 2.00 MeV, but the HEEF lifetimes are noticeably shorter than the VAP lifetimes beyond L shells of 4. The HEEF lifetimes are similar to the VAP lifetimes at 2.35, 3.75 and 3.15 MeV, but again do decay slightly faster at L shells greater than 4. The HEEF observations provide the first calculation of lifetimes at >4 MeV, and comparisons with previous observations at 4.55 MeV are therefore not possible. The fact that the VAP average lifetimes peak further out than the HEEF lifetimes may also in part be due to the VAP lifetimes using L instead of  $L^*$  (e.g., Roederer & Lejosne, 2018).

DESAI ET AL. 12 of 17

At energies of 1.6, 2, 2.3 and 2.75 MeV (Figures 6c–6f), the theory captures the full spread in the HEEF data. At 2.75 MeV, Figure 6g, the theory still bounds the data at L shells greater than 3.5 but at lower radial distances and in the slot region diverges slightly with the prediction at Kp = 4-5 appearing above many of the HEEF lifetimes. This trend is exaggerated further at 3.75 MeV and 4.55, Figures 6h–6g, with the theory predicting longer lifetimes in the slot region than observed and a wide spread in possible lifetimes throughout the outer belt. At 4.55 MeV, the theory predicts even longer lifetimes than at 3.75 MeV, an increase not seen in the HEEF decay rates.

At L shells less than 4, discrepancies between theory and observations have been highlighted to potentially result from the lack of EMIC wave models (He et al., 2023) which preferentially affect larger energies, lower-frequency hiss (Ni et al., 2014) or wave-normal angle effects (Hartley et al., 2018). The EMIC wave models used herein indeed only extend down to  $L^* = 3.25$ , below which these waves are difficult to identify. The discrepancies between the observations and the theory could also well-derive from the assumption in Equation 1 of pure PA diffusion. For example, Ross et al. (2021) employ 3-D modeling to better capture the decay of 2.5 MeV electrons near L = 3.5 using combined energy and radial diffusion. Su et al. (2012) indeed highlight that at L shells greater than 5, the loss timescales are largely insensitive to energy due to radial transport. It is therefore likely that radial diffusion also plays a role at lower L shells and particularly during higher levels of geomagnetic activity when the magnetopause may be more compressed. Broll et al. (2023) also shows that simulated PA diffusion evolves differently than empirical estimates when non-equilibrium PA distributions are considered, and indeed shows this approach yield decay timescales much closer to the observed timescales than the theoretical "lifetimes" (from  $D_{\alpha\alpha}$ 's slowest-decaying mode) in the inner belt.

Although the HEEF lifetimes are well-bounded by the theory, the lifetimes are not strictly ordered by geomagnetic activity, with decays at lower L shells having been highlighted as corresponding to higher Kp indices. An event specific spread in the lifetimes at higher L shells is less apparent but some of the intermediate decays associated with Kp values of 1–3 are still not correctly ordering the decays. This suggests the event specific nature of the decays (Ripoll et al., 2016), potential role of alternative transport processes such as energy and radial diffusion, and errors associated with using a single global geomagnetic activity index for parametrizing radiation belt dynamics.

## 7. Summary and Conclusions

This study has utilized the CRRES-HEEF instrument to analyze relativistic electrons during the maximum of solar cycle 22 with well-resolved measurements extending from 0.65 to 4.55 MeV. The slot region was observed to be flooded with electrons up to at least 4.55 MeV following two severe and one strong geomagnetic storms in the latter half of the mission. Comparable events have only been observed on a few occasions since, for example, during and following the Hallowe'en storm period of 2003 in solar cycle 23 (Baker et al., 2013; Meredith et al., 2009) and during the Mother's day/Gannon storm of May 2024 in solar cycle 25 (Li et al., 2025; Pierrard et al., 2024), with solar cycle 24 identified as possessing an "impenetrable" barrier preventing high energy electrons from reaching below  $L^* = 2.8$  (Baker et al., 2014). The regularity of this phenomenon during the latter half of the mission can therefore only be interpreted as presenting the possibility of reoccurring during sustained periods of elevated solar activity, and therefore representing a direct risk to the increasing number of medium earth orbit satellites operating in, and transiting (Horne & Pitchford, 2015), the slot region.

To examine the individual decay periods in more detail we parameterize the results according to the wide spread in geomagnetic activity during this period. This reveals several important trends. At higher *L* shells, the results are generally well-ordered by geomagnetic activity with high Kp decays often driving shorter loss timescales. Near the inner regions of the outer belt and in the slot region, however, this did not appear to be the case with a series of slow decays corresponding to high levels of activity. These persistent trends suggest that PA diffusion cannot solely explain the evolution of fluxes during this periods, with other competing transport processes, such as energy and radial diffusion, likely contributing. The large geomagnetic storms which flooded the slot region, were also discussed in terms of their severity, with Kp, Dst and an indices often diverging. While the Kp index has been highlighted as better predicting radiation belt dynamics (Borovsky & Shprits, 2017), the lack of strict ordering of electron lifetimes by this index indicates a more sophisticated metric may be better for parametrizing electron lifetimes.

The HEEF electron loss timescales were then compared to lifetimes from other solar cycles and several differences were highlighted. These include longer-lasting sub-MeV electrons near the inner edge of the outer belt, the

DESAI ET AL. 13 of 17

1/doi/10.1029/2025SW004448 by NICE, Natio

several slot-filling events which allowed the first definitive timescales at multi-MeV energies to be derived, and faster decaying fluxes beyond  $L^* \approx 5$ . These differences are associated with higher levels of geomagnetic activity and match similarly elevated sub-MeV lifetimes in this region from solar cycle 23 and 20. This was therefore suggested to result from higher levels of solar and geomagnetic activity during the maximum of solar cycle 22 than VAP observations in cycle 24.

A further outcome of this investigation is that this HEEF data set provided valuable data regarding radiation belt dynamics during the maximum of solar cycle 22, either for stand-alone investigations or boundary conditions for radiation belt modeling. Care should be taken however, particularly when interpreting absolute fluxes, with sight of the underlying energy and PA spectra.

## **Conflict of Interest**

The authors declare no conflicts of interest relevant to this study.

## **Data Availability Statement**

The CRRES-HEEF data set can be accessed on Zenodo at: Johnston et al. (2014a, 2014b). The theoretical diffusion coefficients, loss timescales and PA distributions reported can be accessed on the NERC EDS UK Polar Data Centre at Glauert and Ross (2024).

## References

- Albert, J. M. (1994). Quasi-linear pitch angle diffusion coefficients: Retaining high harmonics. *Journal of Geophysical Research*, 99(A12), 23741–23745. https://doi.org/10.1029/94JA02345
- Albert, J. M. (2005). Evaluation of quasi-linear diffusion coefficients for whistler mode waves in a plasma with arbitrary density ratio. *Journal of Geophysical Research (Space Physics)*, 110(A3), A03218. https://doi.org/10.1029/2004JA010844
- Albert, J. M., & Shprits, Y. Y. (2009). Estimates of lifetimes against pitch angle diffusion. *Journal of Atmospheric and Solar-Terrestrial Physics*, 71(16), 1647–1652. https://doi.org/10.1016/j.jastp.2008.07.004
- Baker, D. N., Jaynes, A. N., Hoxie, V. C., Thorne, R. M., Foster, J. C., Li, X., et al. (2014). An impenetrable barrier to ultrarelativistic electrons in the Van Allen radiation belts. *Nature*, 515(7528), 531–534. https://doi.org/10.1038/nature13956
- Baker, D. N., Kanekal, S. G., Horne, R. B., Meredith, N. P., & Glauert, S. A. (2007). Low-altitude measurements of 2-6 MeV electron trapping lifetimes at 1.5 j L j 2.5. Agu fall meeting abstracts, 2007, SM12A-06.
- Baker, D. N., Kanekal, S. G., Hoxie, V. C., Henderson, M. G., Li, X., Spence, H. E., et al. (2013). A long-lived relativistic electron storage ring embedded in Earth's outer Van Allen Belt. Science, 340(6129), 186–190. https://doi.org/10.1126/science.1233518
- Baker, D. N., Kanekal, S. G., Li, X., Monk, S. P., Goldstein, J., & Burch, J. L. (2004). An extreme distortion of the Van Allen belt arising from the "Hallowe" en solar storm in 2003. *Nature*, 432(7019), 878–881. https://doi.org/10.1038/nature03116
- Benck, S., Mazzino, L., Cyamukungu, M., Cabrera, J., & Pierrard, V. (2010). Low altitude energetic electron lifetimes after enhanced magnetic activity as deduced from sac-c and demeter data. *Annales Geophysicae*, 28(3), 849–859. https://doi.org/10.5194/angeo-28-849-2010
- Blake, J. B., Kolasinski, W. A., Fillius, R. W., & Mullen, E. G. (1992). Injection of electrons and protons with energies of tens of MeV into L<sub>i</sub> 3 on 24 March 1991. *Geophysical Research Letters*, 19(8), 821–824. https://doi.org/10.1029/92GL00624
- Borovsky, J. E., & Shprits, Y. Y. (2017). Is the dst index sufficient to define all geospace storms? *Journal of Geophysical Research: Space Physics*, 122(11), 11543–11547. https://doi.org/10.1002/2017JA024679
- Brautigam, D. H., & Bell, J. T. (1995). Crresele documentation. Environmental Research Papers, 1178. Retrieved from https://apps.dtic.mil/sti/tr/pdf/ADA301770.pdf
- Broll, J. M., Cunningham, G. S., Malaspina, D. M., Claudepierre, S. G., & Ripoll, J.-F. (2023). Inner belt electron decay timescales: A comparison of van Allen probes and dream3d losses following the June 2015 storm. *Geophysical Research Letters*, 50(10), e2022GL102106. https://doi.org/10.1029/2022GL102106(e2022GL1021062022GL102106)
- Burke, W. J., Rubin, A. G., Maynard, N. C., Gentile, L. C., Sultan, P. J., Rich, F. J., et al. (2000). Ionospheric disturbances observed by dmsp at middle to low latitudes during the magnetic storm of June 4–6, 1991. *Journal of Geophysical Research*, 105(A8), 18391–18405. https://doi.org/10.1029/1999JA000188
- Cahill, J. L. J., & Winckler, J. R. (1992). Periodic magnetopause oscillations observed with the GOES satellites on March 24, 1991. *Journal of Geophysical Research*, 97(A6), 8239–8243. https://doi.org/10.1029/92JA00433
- Chen, J.-L., Zou, H., Hao, Y.-X., Ye, Y.-G., Miyoshi, Y., Matsuoka, A., et al. (2024). A sub-relativistic electron three-belt event in the earth's radiation belts: Observation and explanation. *Journal of Geophysical Research: Space Physics*, 129(4), e2023JA032213. https://doi.org/10.1029/2023JA032213
- Cho, M. (2005). Failure mechanisms and protection methods of spacecraft power system. In *Proceedings of the 2005 international symposium on electrical insulating materials (iseim 2005)* (pp. 1–4). IEEE. https://doi.org/10.1109/ISEIM.2005.193320
- Claudepierre, S. G., Ma, Q., & Bortnik, J. (2022). Quantifying radiation belt electron loss processes at L; 4. Journal of Geophysical Research (Space Physics), 127(10), e2022JA030756. https://doi.org/10.1029/2022JA030756
- Claudepierre, S. G., Ma, Q., Bortnik, J., O'Brien, T. P., Fennell, J. F., & Blake, J. B. (2020). Empirically estimated electron lifetimes in the earth's radiation belts: Van allen probe observations. *Geophysical Research Letters*, 47(3), e2019GL086053. https://doi.org/10.1029/2019GL086053
- Cliver, E., Balasubramaniam, K., Nitta, N., & Li, X. (2009). Great geomagnetic storm of 9 November 1991: Association with a disappearing solar filament. *Journal of Geophysical Research*, 114(A3), A00A20. https://doi.org/10.1029/2008ja013232
- Cunningham, G. S., Loridan, V., Ripoll, J.-F., & Schulz, M. (2018). Neoclassical diffusion of radiation-belt electrons across very low 1-shells. Journal of Geophysical Research: Space Physics, 123(4), 2884–2901. https://doi.org/10.1002/2017JA024931

Acknowledgments

J.P. and S.R. acknowledge University of Warwick Undergraduate Research Support Scheme bursaries. RTD acknowledges a Science and Technology Facilities Council Ernest Rutherford Fellowship ST/ W004801/1 and UKSA grant ST/ Y005635/1. NPM and SAG were supported in part by Natural Environment Research Council grants NE/V00249X/1 (Sat-Risk), NE/X000389/1 and NE/ R016038/1. The views expressed are those of the authors and do not necessarily reflect the official policy or position of the Department of the Air Force, the Department of Defense, or the U.S. government. We thank the reviewers and editor for their helpful comments on this manuscript.

DESAI ET AL. 14 of 17

- Desai, R. T., Eastwood, J. P., Horne, R. B., Allison, H. J., Allanson, O., Watt, C. E. J., et al. (2021). Drift orbit bifurcations and cross-field transport in the outer radiation belt: Global mhd and integrated test-particle simulations. *Journal of Geophysical Research: Space Physics*, 126(10), e2021JA029802. https://doi.org/10.1029/2021JA029802
- Desai, R. T., Freeman, M. P., Eastwood, J. P., Eggington, J. W. B., Archer, M. O., Shprits, Y. Y., et al. (2021). Interplanetary shock-induced magnetopause motion: Comparison between theory and global magnetohydrodynamic simulations. *Geophysical Research Letters*, 48(16), e2021GL092554. https://doi.org/10.1029/2021GL092554
- Dichter, B., & Hanser, F. (1995). Analyze data from crres payloads afgl-701/dosimeter and afgl- 701-4/fluxmeter. PL-TR-92-2223, Phillips Laboratory, AFMC (pp. 1–29). Hanscom AFB. (ADA241399).
- Dichter, B., Hanser, F., Sellers, B., & Hunerwadel, J. (1993). High energy electron fluxmeter. *IEEE Transactions on Nuclear Science*, 40(2), 252–255. https://doi.org/10.1109/23.212350
- Elkington, S. R., Wiltberger, M., Chan, A. A., & Baker, D. N. (2004). Physical models of the geospace radiation environment. *Journal of Atmospheric and Solar-Terrestrial Physics*, 66(15–16), 1371–1387. https://doi.org/10.1016/j.jastp.2004.03.023
- Elphic, R. C., Thomsen, M. F., Moore, K. R., M, D. J., & Bame, S. J. (1991). Geosynchronous observations of the Magnetopause and related Phenomena on March 24 and 25, 1991. AGU Fall Meeting December 9-13, 8(9–10), 319.
- Fok, M.-C., Moore, T. E., & Spjeldvik, W. N. (2001). Rapid enhancement of radiation belt electron fluxes due to substorm dipolarization of the geomagnetic field. JGR, 106(A3), 3873–3882. https://doi.org/10.1029/2000JA000150
- Gao, Y., Yang, D., & Zhang, G. (1997). The geomagnetic disturbance of June, 1991: The characteristics on the ground and at the geosynchronous altitude. Chinese Journal of Space Science, 17(1), 64. https://doi.org/10.11728/cjss1997.01.064
- Ginet, G. P., O'Brien, T. P., Huston, S. L., Johnston, W. R., Guild, T. B., Friedel, R., et al. (2013). AE9, AP9 and SPM: New models for specifying the trapped energetic particle and space plasma environment. Space Science Reviews, 179(1–4), 579–615. https://doi.org/10.1007/s11214-013-9964-y
- Glauert, S., & Ross, J. (2024). Pitch angle distributions, loss timescales and diffusion coefficients for the earth's radiation belts. NERC EDS UK Polar Data Centre. https://doi.org/10.5285/6d20ed7b-59e1-4284-a6f2-3e2589da6d2a
- Glauert, S. A., Atkinson, J. W., Ross, J. P., & Horne, R. B. (2024). A new model of Electron Pitch angle distributions and loss timescales in the Earth's radiation belts. *Journal of Geophysical Research (Space Physics)*, 129(6), e2023JA032249. https://doi.org/10.1029/2023JA032249
- Glauert, S. A., & Horne, R. B. (2005). Calculation of pitch angle and energy diffusion coefficients with the PADIE code. *Journal of Geophysical Research (Space Physics)*, 110(A4), A04206. https://doi.org/10.1029/2004JA010851
- Glauert, S. A., Horne, R. B., & Meredith, N. P. (2014). Three-dimensional electron radiation belt simulations using the BAS radiation Belt model with new diffusion models for chorus, plasmaspheric hiss, and lightning-generated whistlers. *Journal of Geophysical Research (Space Physics)*, 119(1), 268–289. https://doi.org/10.1002/2013JA019281
- Glauert, S. A., Horne, R. B., & Meredith, N. P. (2018). A 30-year simulation of the outer electron radiation belt. Space Weather, 16(10), 1498–1522. https://doi.org/10.1029/2018SW001981
- Green, A., Li, W., Ma, Q., Shen, X.-C., Bortnik, J., & Hospodarsky, G. B. (2020). Properties of lightning generated whistlers based on van allen probes observations and their global effects on radiation belt electron loss. *Geophysical Research Letters*, 47(17), e2020GL089584. https://doi.org/10.1029/2020GL089584
- Gussenhoven, M., Mullen, E., & Brautigam, D. (1996). Improved understanding of the earth's radiation belts from the crres satellite. *IEEE Transactions on Nuclear Science*, 43(2), 353–368. https://doi.org/10.1109/23.490755
- Hands, A. D. P., Ryden, K. A., Meredith, N. P., Glauert, S. A., & Horne, R. B. (2018). Radiation effects on satellites during extreme space weather events. Space Weather, 16(9), 1216–1226. https://doi.org/10.1029/2018SW001913
- Hanser, F. (1995). Data analysis procedures for the crres payloads afgl-701-2/dosimeter and agrl-701-4/fluxmeter and application of the data analysis results to improve the static and dynamic models of the earth's radiation belts. Hanscom AFB. PL-TR-92-2223, Phillips Laboratory, AFMC
- Hartley, D. P., Kletzing, C. A., Santolík, O., Chen, L., & Horne, R. B. (2018). Statistical properties of plasmaspheric hiss from van allen probes observations. *Journal of Geophysical Research: Space Physics*, 123(4), 2605–2619. https://doi.org/10.1002/2017JA024593
- He, Z., Xu, J., Wang, C., Dai, L., Ni, B., & Roth, I. (2023). Evidence of h+-band emic waves in the inner radiation belt observed by van allen probes during magnetic storms. *Journal of Geophysical Research: Space Physics*, 128(3), e2022JA031088. https://doi.org/10.1029/
- Horne, R. B., & Pitchford, D. (2015). Space weather concerns for all-electric propulsion satellites. Space Weather, 13, 430–433. https://doi.org/10.1002/2015SW001198
- Hudson, M. K., Elkington, S. R., Lyon, J. G., Marchenko, V. A., Roth, I., Temerin, M., et al. (1997). Simulations of radiation belt formation during storm sudden commencements. *Journal of Geophysical Research*, 102(A7), 14087–14102. https://doi.org/10.1029/97JA03995
- Ishikawa, H., Miyake, W., & Matsuoka, A. (2013). Variation of proton radiation belt deduced from solar cell degradation of akebono satellite. *Earth Planets and Space*, 65(2), 121–125, https://doi.org/10.5047/eps.2012.06.004
- Johnston, W., Lindstrom, C., & Ginet, G. (2014a). Crres medium electron sensor a (mea) and high energy electron fluxmeter (heef): Cross-calibrated data set. Zenodo. https://doi.org/10.5281/zenodo.15547414
- Johnston, W. R., Lindstrom, C. D., & Ginet, G. P. (2010). Characterization of radiation belt electron energy spectra from CRRES observations. In *Agu fall meeting abstracts* (Vol. 2010, pp. SM33C–1925).
- Johnston, W. R., Lindstrom, C. D., & Ginet, G. P. (2014b). Crres medium electron sensor a (mea) and high energy electron fluxmeter (heef): Cross-calibrated data set description. Air Force research laboratory space vehicles directorate 3550 Aberdeen Avenue SE Kirtland AFB, NM 87117-5776. Retrieved from https://apps.dtic.mil/sti/pdfs/ADA604519.pdfdoi:AFRL-RV-PS-TR-2014-0016
- Kellerman, A. C., Shprits, Y. Y., Kondrashov, D., Subbotin, D., Makarevich, R. A., Donovan, E., & Nagai, T. (2014). Three-dimensional data assimilation and reanalysis of radiation belt electrons: Observations of a four-zone structure using five spacecraft and the verb code. *Journal of Geophysical Research: Space Physics*, 119(11), 8764–8783. https://doi.org/10.1002/2014JA020171
- Kennel, C. F., Edmiston, J. P., & Hada, T. (1985). A quarter century of collisionless shock research. Washington DC American Geophysical Union Geophysical Monograph Series, 34, 1–36. https://doi.org/10.1029/GM034p0001
- Koehn, G. J., Desai, R. T., Davies, E. E., Forsyth, R. J., Eastwood, J. P., & Poedts, S. (2022). Successive interacting coronal mass ejections: How to create a perfect storm. *ApJ*, 941(2), 139. https://doi.org/10.3847/1538-4357/aca28c
- Lauben, D. S., Inan, U. S., & Bell, T. F. (2001). Precipitation of radiation belt electrons induced by obliquely propagating lightning-generated whistlers. *Journal of Geophysical Research*, 106(A12), 29745–29770. https://doi.org/10.1029/1999JA000155
- Li, X., Roth, I., Temerin, M., Wygant, J. R., Hudson, M. K., & Blake, J. B. (1993). Simulation of the prompt energization and transport of radiation belt particles during the March 24, 1991 ssc. *Geophysical Research Letters*, 20(22), 2423–2426. https://doi.org/10.1029/93GL02701

DESAI ET AL. 15 of 17

**Space Weather** 

- Li, X., Xiang, Z., Mei, Y., O'Brien, D., Brennan, D., Zhao, H., et al. (2025). A new electron and proton radiation belt identified by cirbe/reptile-2 measurements after the magnetic super storm of 10 May 2024. *Journal of Geophysical Research: Space Physics*, 130(2), e2024JA033504. https://doi.org/10.1029/2024JA033504
- Loewe, C. A., & Prölss, G. W. (1997). Classification and mean behavior of magnetic storms. *Journal of Geophysical Research*, 102(A7), 14209–14213. https://doi.org/10.1029/96JA04020
- Lozinski, A. R., Kellerman, A. C., Bortnik, J., Horne, R. B., Desai, R. T., & Glauert, S. A. (2025). Modeling the internal redistribution of Earth's proton radiation belt by interplanetary shocks. *Journal of Geophysical Research: Space Physics*, 130, e2025JA033871. https://doi.org/10.1029/2025JA033871
- Lyons, L. R. (1974). General relations for resonant particle diffusion in pitch angle and energy. *Journal of Plasma Physics*, 12(1), 45–49. https://doi.org/10.1017/S0022377800024910
- Lyons, L. R., Thorne, R. M., & Kennel, C. F. (1972). Pitch-angle diffusion of radiation belt electrons within the plasmasphere. *JGR*, 77(19), 3455–3474. https://doi.org/10.1029/JA077i019p03455
- Ma, Q., Li, W., Thorne, R. M., Bortnik, J., Kletzing, C. A., Kurth, W. S., & Hospodarsky, G. B. (2016). Electron scattering by magnetosonic waves in the inner magnetosphere. *Journal of Geophysical Research: Space Physics*, 121(1), 274–285. https://doi.org/10.1002/2015JA021992
- Mann, I. R., Ozeke, L. G., Murphy, K. R., Claudepierre, S. G., Turner, D. L., Baker, D. N., et al. (2016). Explaining the dynamics of the ultra-relativistic third Van Allen radiation belt. *Nature Physics*, 12(10), 978–983. https://doi.org/10.1038/nphys3799
- McComas, D. J., Angold, N., Elliott, H. A., Livadiotis, G., Schwadron, N. A., Skoug, R. M., & Smith, C. W. (2013). Weakest solar wind of the space age and the current "mini" solar maximum. ApJ, 779(1), 2. https://doi.org/10.1088/0004-637X/779/1/2
- McKellar, B. (1996). Unfolding the high energy electron flux from CRRES fluxmeter measurements PhD Thesis. Air Force Institute of Technology Air University. AFIT/GAP7ENP796D-8.
- Meredith, N. P., Horne, R. B., Glauert, S. A., & Anderson, R. R. (2007). Slot region electron loss timescales due to plasmaspheric hiss and lightning-generated whistlers. *Journal of Geophysical Research*, 112(A8), A08214. https://doi.org/10.1029/2007JA012413
- Meredith, N. P., Horne, R. B., Glauert, S. A., Baker, D. N., Kanekal, S. G., & Albert, J. M. (2009). Relativistic electron loss timescales in the slot region. *Journal of Geophysical Research (Space Physics)*, 114(A3), A03222. https://doi.org/10.1029/2008JA013889
- Meredith, N. P., Horne, R. B., Glauert, S. A., Thorne, R. M., Summers, D., Albert, J. M., & Anderson, R. R. (2006). Energetic outer zone electron loss timescales during low geomagnetic activity. *Journal of Geophysical Research (Space Physics)*, 111(A5), A05212. https://doi.org/10.1029/
- Meredith, N. P., Horne, R. B., Kersten, T., Li, W., Bortnik, J., Sicard, A., & Yearby, K. H. (2018). Global model of plasmaspheric hiss from multiple satellite observations. *Journal of Geophysical Research: Space Physics*, 123(6), 4526–4541. https://doi.org/10.1029/2018JA025226
- Meredith, N. P., Horne, R. B., Shen, X.-C., Li, W., & Bortnik, J. (2020). Global model of whistler mode chorus in the near-equatorial region (lλml 18°). *Geophysical Research Letters*, 47(11), e2020GL087311. https://doi.org/10.1029/2020GL087311
- Miyoshi, Y., Sakaguchi, K., Shiokawa, K., Evans, D., Albert, J., Connors, M., & Jordanova, V. (2008). Precipitation of radiation belt electrons by emic waves, observed from ground and space. *Geophysical Research Letters*, 35(23), L23101. https://doi.org/10.1029/2008GL035727
- Mullen, E. G., Gussenhoven, M. S., Ray, K., & Violet, M. (1991). A double-peaked inner radiation belt Cause and effect as seen on CRRES. IEEE Transactions on Nuclear Science, 38(6), 1713–1717. https://doi.org/10.1109/23.124167
- Ni, B., Li, W., Thorne, R. M., Bortnik, J., Ma, Q., Chen, L., et al. (2014). Resonant scattering of energetic electrons by unusual low-frequency hiss. Geophysical Research Letters, 41(6), 1854–1861. https://doi.org/10.1002/2014GL059389
- NOAA Space Environment Center. (2004). *Intense space weather storms, October 19 November 07, 2003*. Tech. Rep. National Oceanic and Atmospheric Administration. Retrieved from https://www.weather.gov/media/publications/assessments/SWstorms\_assessment.pdf
- O'Brien, T. P., Looper, M. D., & Blake, J. B. (2008). Eigenmode analysis of pitch-angle diffusion of energetic electrons in the outer zone. *Journal of Geophysical Research*, 113(A8). https://doi.org/10.1016/j.jastp.2008.05.011
- Olson, W. P., & Pfitzer, K. A. (1977). Magnetospheric magnetic field modeling. annual scientific report (Tech. Rep.). McDonnell Douglas Astronautics Co. Retrieved from https://www.osti.gov/biblio/7212748
- Orsolini, Y. J., Manney, G. L., Santee, M. L., & Randall, C. E. (2005). An upper stratospheric layer of enhanced hno3 following exceptional solar storms. Geophysical Research Letters, 32(12), L12S01. https://doi.org/10.1029/2004GL021588
- Ozhogin, P., Tu, J., Song, P., & Reinisch, B. W. (2012). Field-aligned distribution of the plasmaspheric electron density: An empirical model derived from the image rpi measurements. *Journal of Geophysical Research*, 117(A6), A06225. https://doi.org/10.1029/2011JA017330
- Pierrard, V., Winant, A., Botek, E., & Péters de Bonhome, M. (2024). The mother's day solar storm of 11 May 2024 and its effect on Earth's radiation belts. *Universe*, 10(10), 391. https://doi.org/10.3390/universe10100391
- Pinto, V. A., Bortnik, J., Moya, P. S., Lyons, L. R., Sibeck, D. G., Kanekal, S. G., et al. (2018). Characteristics, occurrence, and decay rates of remnant belts associated with three-belt events in the earth's radiation belts. *Geophysical Research Letters*, 45(22), 12099–12107. https://doi.org/10.1029/2018GL080274
- Reeves, G. D., Chen, Y., Cunningham, G. S., Friedel, R. W. H., Henderson, M. G., Jordanova, V. K., et al. (2012). Dynamic radiation environment assimilation model: Dream. *Space Weather*, 10(3), 03006. https://doi.org/10.1029/2011SW000729
- Ripoll, J. F., Albert, J. M., & Cunningham, G. S. (2014). Electron lifetimes from narrowband wave-particle interactions within the plasmasphere. Journal of Geophysical Research (Space Physics), 119(11), 8858–8880. https://doi.org/10.1002/2014JA020217
- Ripoll, J.-F., Chen, Y., Fennell, J. F., & Friedel, R. H. W. (2015). On long decays of electrons in the vicinity of the slot region observed by heo3. Journal of Geophysical Research: Space Physics, 120(1), 460–478. https://doi.org/10.1002/2014JA020449
- Ripoll, J.-F., Reeves, G. D., Cunningham, G. S., Loridan, V., Denton, M., Santolík, O., et al. (2016). Reproducing the observed energy-dependent structure of earth's electron radiation belts during storm recovery with an event-specific diffusion model. *Geophysical Research Letters*, 43(11), 5616–5625. https://doi.org/10.1002/2016GL068869
- Roble, R. G., & Rees, M. H. (1977). Time-dependent studies of the Aurora: Effects of particle precipitation on the dynamic morphology of ionospheric and atmospheric properties. PSS, 25(11), 991–1010. https://doi.org/10.1016/0032-0633(77)90146-5
- Roederer, J. G. (1970). Dynamics of geomagnetically trapped radiation.
- Roederer, J. G., & Lejosne, S. (2018). Coordinates for representing radiation belt particle flux. *Journal of Geophysical Research (Space Physics)*, 123(2), 1381–1387. https://doi.org/10.1002/2017JA025053
- Ross, J. P. J., Glauert, S. A., Horne, R. B., Watt, C. E., Meredith, N. P., & Woodfield, E. E. (2020). A new approach to constructing models of electron diffusion by emic waves in the radiation belts. *Geophysical Research Letters*, 47(20), e2020GL088976. https://doi.org/10.1029/2020GL088976
- Ross, J. P. J., Glauert, S. A., Horne, R. B., Watt, C. E. J., & Meredith, N. P. (2021). On the variability of EMIC waves and the consequences for the relativistic electron radiation belt population. *Journal of Geophysical Research (Space Physics)*, 126(12), e29754. https://doi.org/10.1029/2021JA029754

DESAI ET AL. 16 of 17

- Ross, J. P. J., Meredith, N. P., Glauert, S. A., Horne, R. B., & Clilverd, M. A. (2019). Effects of vlf transmitter waves on the inner belt and slot region. *Journal of Geophysical Research: Space Physics*, 124(7), 5260–5277. https://doi.org/10.1029/2019JA026716
- Schulz, M., & Lanzerotti, L. J. (1974). Particle diffusion in the radiation belts (Vol. 7). Springer-Verlag. https://doi.org/10.1007/978-3-642-65675-0
- Seki, K., Miyoshi, Y., Summers, D., & Meredith, N. P. (2005). Comparative study of outer-zone relativistic electrons observed by akebono and crres. Journal of Geophysical Research, 110(A2), A02203. https://doi.org/10.1029/2004JA010655
- Selesnick, R. S. (2016). Stochastic simulation of inner radiation belt electron decay by atmospheric scattering. *Journal of Geophysical Research:* Space Physics, 121(2), 1249–1262. https://doi.org/10.1002/2015JA022180
- Selesnick, R. S., Looper, M. D., & Mewaldt, R. A. (2007). A theoretical model of the inner proton radiation belt. Space Weather, 5(4), S04003. https://doi.org/10.1029/2006SW000275
- Shea, M. A., & Smart, D. F. (1993). March 1991 solar-terrestrial phenomena and related technological consequences. In E. V. Benton, J. H. Adams, & M. I. Panasyuk (Eds.), Space radiation environment: Empirical and physical models. Dubna.
- Shprits, Y. Y., Meredith, N. P., & Thorne, R. M. (2007). Parameterization of radiation belt electron loss timescales due to interactions with chorus waves. Geophysical Research Letters, 34(11), L11110. https://doi.org/10.1029/2006GL029050
- Shprits, Y. Y., Subbotin, D., & Ni, B. (2009). Evolution of electron fluxes in the outer radiation belt computed with the VERB code. *Journal of Geophysical Research (Space Physics)*, 114(A11), A11209. https://doi.org/10.1029/2008JA013784
- Shprits, Y. Y., Thorne, R. M., Friedel, R., Reeves, G. D., Fennell, J., Baker, D. N., & Kanekal, S. G. (2006). Outward radial diffusion driven by losses at magnetopause. *Journal of Geophysical Research*, 111(A11), A11214. https://doi.org/10.1029/2006JA011657
- Sibeck, D. G., McEntire, R. W., Lui, A. T. Y., Lopez, R. E., & Krimigis, S. M. (1987). Magnetic field drift shell splitting: Cause of unusual dayside particle pitch angle distributions during storms and substorms. *Journal of Geophysical Research*, 92(A12), 13485–13497. https://doi.org/10.1029/JA092iA12p13485
- Su, Y.-J., Johnston, W. R., Albert, J. M., Ginet, G. P., Starks, M. J., & Roth, C. J. (2012). Scatha measurements of electron decay times at 5 ¡ 1 ¡ 8. Journal of Geophysical Research, 117(A8), A08212. https://doi.org/10.1029/2012JA017685
- Su, Z., Xiao, F., Zheng, H., & Wang, S. (2010). STEERB: A three-dimensional code for storm-time evolution of electron radiation belt. *Journal of Geophysical Research (Space Physics)*, 115(A9), A09208, https://doi.org/10.1029/2009JA015210
- Summers, D., Ma, C., & Mukai, T. (2004). Competition between acceleration and loss mechanisms of relativistic electrons during geomagnetic storms. *Journal of Geophysical Research (Space Physics)*, 109(A4), A04221. https://doi.org/10.1029/2004JA010437
- Summers, D., Ni, B., Meredith, N. P., Horne, R. B., Thorne, R. M., Moldwin, M. B., & Anderson, R. R. (2008). Electron scattering by whistler-mode ELF hiss in plasmaspheric plumes. *Journal of Geophysical Research (Space Physics)*, 113(A4), A04219. https://doi.org/10.1029/
- Vampola, A. L. (1971). Natural variations in the geomagnetically trapped electron population. In E. A. Warman (Ed.), Proceedings of the national symposium on natural and manmade radiation in Space, Aerospace Corp (pp. 539–547). El Segundo.
- Vampola, A. L., Osborn, J. V., & Johnson, B. M. (1992). CRRES magnetic electron spectrometer AFGL-701-5A (MEA). Journal of Spacecraft and Rockets, 29(4), 592–595. https://doi.org/10.2514/3.25504
- van Allen, J. A. (1959). The geomagnetically trapped corpuscular radiation. *JGR*, 64(11), 1683–1689. https://doi.org/10.1029/JZ064i011p01683
  Vennerstrom, S., Lefevre, L., Dumbović, M., Crosby, N., Malandraki, O., Patsou, I., et al. (2016). Extreme geomagnetic storms–1868–2010. *Solar Physics*, 291(5), 1447–1481. https://doi.org/10.1007/s11207-016-0897-y
- Wang, D., & Shprits, Y. Y. (2019). On how high-latitude chorus waves tip the balance between acceleration and loss of relativistic electrons. Geophysical Research Letters, 46(14), 7945–7954. https://doi.org/10.1029/2019GL082681
- Wang, D., Shprits, Y. Y., Haas, B., & Drozdov, A. Y. (2024). Improved lifetime model of energetic electrons due to their interactions with chorus waves. *Geophysical Research Letters*, 51(19), e2023GL107991. https://doi.org/10.1029/2023GL107991
- West, H. I., Jr., Buck, R. M., & Davidson, G. T. (1981). The dynamics of energetic electrons in the earth's outer radiation belt during 1968 as observed by the lawrence livermore national laboratory's spectrometer on ogo 5. *Journal of Geophysical Research*, 86(A4), 2111–2142. https://doi.org/10.1029/JA086iA04p02111
- Wilson, G. R., Burke, W. J., Maynard, N. C., Huang, C. Y., & Singer, H. J. (2001). Global electrodynamics observed during the initial and main phases of the July 1991 magnetic storm. *Journal of Geophysical Research*, 106(A11), 24517–24539. https://doi.org/10.1029/2000JA000348
- Wong, J.-M., Meredith, N. P., Horne, R. B., Glauert, S. A., & Ross, J. P. J. (2022). Electron diffusion by magnetosonic waves in the earth's radiation belts. *Journal of Geophysical Research: Space Physics*, 127(4), e2021JA030196. https://doi.org/10.1029/2021JA030196
- Zhao, H., Johnston, W. R., Baker, D. N., Li, X., Ni, B., Jaynes, A. N., et al. (2019). Characterization and evolution of radiation belt electron energy spectra based on the van allen probes measurements. *Journal of Geophysical Research: Space Physics*, 124(6), 4217–4232. https://doi.org/10.1029/2019JA026697

DESAI ET AL. 17 of 17